

1 Fast dimension-reduced climate model calibration

2 Won Chang, Murali Haran, Roman Olson, and Klaus Keller

3 March 22, 2022

4 **Abstract**

5 What is the response of the climate system to anthropogenic forcings?
6 This question is addressed typically using projections from climate models.
7 The uncertainty surrounding current climate projections has important pol-
8 icy implications. Characterizing and, if possible, reducing this uncertainty
9 is an area of ongoing research. We consider the problem of making pro-
10 jections of the North Atlantic meridional overturning circulation (AMOC).
11 AMOC projections are of interest because AMOC changes may considerably
12 impact natural and human systems. Uncertainties about climate model
13 parameters play a key role in uncertainties in AMOC projections. When
14 the observational data and the climate model output are high-dimensional
15 spatial data sets, the data are typically aggregated due to computational
16 constraints. The effects of aggregation are unclear because statistically rig-
17 orous approaches for model parameter inference have been infeasible for
18 high-resolution data. Here we develop a flexible and computationally effi-
19 cient approach using principal components and basis expansions to study the
20 effect of spatial data aggregation on parametric and projection uncertainties.
21 Our Bayesian reduced-dimensional calibration approach allows us to study
22 the effect of complicated error structures and data-model discrepancies on

23 our ability to learn about climate model parameters from high-dimensional
24 data. Considering high-dimensional spatial observations reduces the effect
25 of deep uncertainty associated with different priors and results in sharper
26 projections based on our climate model. We demonstrate that our com-
27 putationally efficient approach may be widely applicable to a variety of
28 high-dimensional computer model calibration problems.

29 **1 Introduction**

30 Computer models play an important role in understanding complex physical pro-
31 cesses in modern science and engineering. They are particularly important in cli-
32 mate science where climate models, complex deterministic systems used to model
33 climate processes, are used both to study climate phenomena as well as make pro-
34 jections about future climate. A major source of uncertainty in climate projections
35 is due to uncertainties about model parameters. Calibration of the parameters us-
36 ing observational data is hence one avenue to reduce the uncertainty in future
37 projections. A number of issues and challenges arise when performing statisti-
38 cal calibration of model parameters. Because each run of the computer model
39 is computationally expensive, computer model output is typically obtained for a
40 relatively small sample of parameter values. Furthermore, the model output at
41 each parameter setting may be high-dimensional and in the form of spatial fields.
42 A sound statistical approach to this problem therefore needs to simultaneously
43 address the spatial dependence in the data and model outputs, account for various
44 sources of uncertainty, and remain computationally efficient.

45 Previous approaches for climate model calibration have relied on heavy data

46 aggregation, turning three-dimensional data into two or one-dimensional data (e.g.
47 Sanso and Forest, 2009; Goes et al., 2010; Olson et al., 2012) largely due to compu-
48 tational considerations (cf. Schmittner et al., 2009). An important and interesting
49 question is what information, if any, is lost by this data aggregation. This is a
50 largely unanswered question due to the inability of existing methods to analyze
51 large spatial data sets of both computer model output and observations. Through-
52 out this manuscript we will use “large” to refer to data sets that comprise over
53 tens of thousands of spatial observations. Here we develop a computationally effi-
54 cient approach that handles large data sets. This approach gives us the freedom to
55 carry out a careful study of the effects of data aggregation, for example comparing
56 calibration based on unaggregated three-dimensional data with calibration based
57 on aggregated two-dimensional data. Our approach also enables to investigate
58 the interaction between data aggregation and data-model discrepancies and errors
59 when inferring computer model parameters. Our study addresses the questions of
60 (i) whether aggregation is harmful or helpful, and (ii) how observations may be
61 collected and processed in order to calibrate climate models and make projections
62 with them.

63 We adopted a Gaussian process based approach to the calibration problem
64 (Sacks et al., 1989; Kennedy and O’Hagan, 2001). Gaussian processes provide flex-
65 ible statistical interpolators or “emulators” of the computer model across various
66 parameter settings and are therefore attractive for climate model calibration (cf.
67 Sanso and Forest, 2009; Bhat et al., 2012). Unfortunately, the likelihood evalua-
68 tions involved in fitting such models can become prohibitive with high-dimensional
69 spatial data due to the expensive matrix operations involved. Current approaches
70 for high-dimensional computer model calibration can reduce the computational

71 burden and make likelihood evaluation feasible for moderately large datasets (spa-
72 tial fields observed at a few thousand locations) or datasets that are on a regular
73 and complete grid (Higdon et al., 2008; Bhat et al., 2012; Bayarri et al., 2007).
74 However, to the best of our knowledge, no current calibration approach can over-
75 come the computational challenge of dealing with large spatial data sets on a
76 highly irregular grid.

77 The scientific problem motivating the statistical analysis is to project the future
78 state of the North Atlantic meridional overturning circulation (AMOC) in response
79 to anthropogenic climate forcing. The AMOC is a large-scale ocean circulation
80 that transports cold and dense water equatorward in deep North Atlantic, and
81 warm and salty water poleward in the upper layers of North Atlantic. The AMOC
82 might show a persistent weakening in response to anthropogenic forcing. Because
83 the AMOC plays an important role in heat and carbon transport, an AMOC
84 weakening is projected to have considerable impacts on climate, and, in response,
85 on natural and human systems (cf. Alley et al., 2007; Keller et al., 2005, 2007).
86 We use previously published ensemble runs of the University of Victoria Earth
87 System Climate Model (UVic ESCM) (Weaver et al., 2001) to set up an example
88 calibration problem. Vertical ocean mixing is important in projecting the AMOC
89 (Wunsch and Ferrari, 2004), but much of the mixing occurs on scales below that
90 of the UVic ESCM, hence mixing is “parameterized” (cf. Weaver et al., 2001;
91 Schmittner et al., 2009; Goes et al., 2010) using a “vertical background diffusivity”
92 (K_{bg}). The AMOC projections depend on the K_{bg} parameter values (e.g. Goes
93 et al., 2010). The value of K_{bg} is uncertain; it therefore needs to be calibrated
94 using observations of the climate that are informative about K_{bg} (cf. Goes et al.,
95 2010; Bhat et al., 2012).

96 Here, we calibrate K_{bg} using observations of ocean potential temperature from
97 World Ocean Atlas 2009 (Antonov et al., 2010; Locarnini et al., 2010). K_{bg} affects
98 the depth of the oceanic pycnocline (Gnanadesikan, 1999) and the AMOC (Bryan,
99 1987; Goes et al., 2010). As a consequence, models with different K_{bg} values are
100 expected to result in different ocean temperature distributions. Ocean tempera-
101 tures are therefore informative about K_{bg} . We provide a detailed description of the
102 data in Section 4. Note that both the UVic ESCM output and the observational
103 data are spatial data sets with more than 60,000 spatial locations. Of particular
104 interest is how data aggregation affects the calibration result for K_{bg} . Often ob-
105 servations of climate and climate model outputs are 3-D spatial fields. When the
106 spatial data sets are large it is common practice to aggregate them into 1-D or 2-D
107 patterns (i.e. Sanso and Forest, 2009; Drignei et al., 2008; Forest et al., 2008; Goes
108 et al., 2010; Bhat et al., 2012) either to avoid computational issues or because the
109 skill of the models at higher resolution may not always be trusted.

110 We describe a new approach that enables calibration with large spatial data
111 sets without doing data aggregation. While our methodology has been devel-
112 oped in the context of high-dimensional spatial fields, it applies more generally.
113 In our simulated examples, we have shown that the method can handle compli-
114 cated model-observation discrepancy processes without sacrificing computational
115 efficiency. Our study suggests that data aggregation can cause considerable infor-
116 mation loss. Reducing the data aggregation can enable valuable new insights and
117 considerably reduce parametric and projection uncertainty.

118 The remainder of this paper is organized as follows. In Section 2 we describe
119 our two-stage framework for climate model calibration and the associated compu-
120 tational challenges. In Section 3 we propose a general model calibration approach

121 in a reduced dimensional space that uses a combination of principal components
122 and a basis representation to overcome the computational challenges. In Section
123 4 we describe the data and provide implementation details and in Section 5 we
124 discuss the results from simulated examples and real data. We conclude this paper
125 with caveats and future directions in Section 6.

126 **2 Model Calibration Framework**

127 Our computer model calibration framework consists of two stages, (i) model emu-
128 lation and (ii) parameter calibration (Bayarri et al., 2007; Bhat et al., 2012). First,
129 we construct an emulator that interpolates computer model outputs at different
130 parameter settings using Gaussian random fields (Sacks et al., 1989). This can
131 be viewed as statistical interpolation or “kriging” (Cressie, 1994) in the computer
132 model parameter space. Second, we infer the computer model parameters by re-
133 lating observational data to computer model output using the emulator, while
134 considering observational error and allowing for systematic discrepancies between
135 the model and observations (Kennedy and O’Hagan, 2001). Note that this two-
136 stage approach has some advantages over fully Bayesian methods that combine the
137 two stages into a single inferential step. By ‘cutting feedback’ or modularization
138 (Rougier, 2008; Bhat et al., 2012; Liu et al., 2009), this two-stage approach ensures
139 that inference in the emulation stage is not contaminated by model discrepancy
140 and observational error. In addition, separating the emulation stage from calibra-
141 tion provides an easier way to diagnose the accuracy of an emulator. Furthermore,
142 computations are faster and parameter identifiability problems are reduced.

143 Let $Y(\mathbf{s}, \boldsymbol{\theta})$ denote the computer model output at the spatial location $\mathbf{s} =$

144 (longitude, latitude, depth) $\in \mathcal{S} \subseteq \mathbb{R}^3$ and the model parameter setting $\boldsymbol{\theta} \in \Theta \subseteq$
 145 \mathbb{R}^3 , where \mathcal{S} is the spatial domain of the process and Θ is the computer model
 146 parameter space. $Z(\mathbf{s})$ is the corresponding observation at the spatial location \mathbf{s} .
 147 Since each run of the climate model is computationally expensive, we can obtain
 148 computer model outputs only for a relatively small number of design points p .
 149 We denote these design points in the parameter space by $\boldsymbol{\theta}_1, \dots, \boldsymbol{\theta}_p \in \mathcal{D} \subseteq \mathbb{R}^3$.
 150 Let $\mathbf{Y}_i \in \mathbb{R}^n$ be the computer model output at each parameter setting $\boldsymbol{\theta}_i$ for
 151 $i = 1, \dots, p$. Each computer model output $\mathbf{Y}_i = (Y(\mathbf{s}_1, \boldsymbol{\theta}_i), \dots, Y(\mathbf{s}_n, \boldsymbol{\theta}_i))^T$ is a
 152 spatial process observed at n different spatial locations $(\mathbf{s}_1, \dots, \mathbf{s}_n)$. Let \mathbf{Y} be the
 153 vector of concatenated computer model outputs such that $\mathbf{Y} = (\mathbf{Y}_1, \dots, \mathbf{Y}_p)^T$. We
 154 also denote the observed spatial process at n locations by $\mathbf{Z} = (Z(\mathbf{s}_1), \dots, Z(\mathbf{s}_n))^T$.
 155 Note that we assume that the locations for each model output and observation data
 156 are the same. If they are different, one can interpolate either of them depending
 157 on which one has a higher resolution. Our objective is to infer the parameter $\boldsymbol{\theta}$ by
 158 combining information from \mathbf{Z} and \mathbf{Y} .

159 2.1 Two-Stage Emulation and Calibration

160 We first outline our general framework for emulation and calibration.

161 Model Emulation Using Gaussian Random Fields

Following Bhat et al. (2012) we approximate the climate model using a Gaussian process such that

$$\mathbf{Y} \sim N(\mu_{\boldsymbol{\beta}}, \Sigma(\boldsymbol{\xi}_y)),$$

162 where μ_{β} is a linear mean function $\mathbf{X}\beta$ with a $np \times b$ covariate matrix \mathbf{X} and a
 163 vector of regression coefficient β . The covariates in \mathbf{X} are the spatial locations
 164 (e.g. latitude, longitude, and depth) and the climate parameters. The covariate
 165 matrix \mathbf{X} contains all the spatial coordinates and the parameter settings used to
 166 define the covariance matrix $\Sigma(\xi_y)$. ξ_y is a vector of parameters determining the
 167 covariance matrix $\Sigma(\xi_y)$. We fit a Gaussian random field to \mathbf{Y} by finding the
 168 maximum likelihood estimate (MLE) of (β, ξ_y) , denoted by $(\hat{\beta}, \hat{\xi}_y)$.

169 The fitted Gaussian random field defines the probability model for the com-
 170 puter model output at any location $\mathbf{s} \in \mathcal{S}$ and parameter setting $\theta \in \Theta$. Therefore,
 171 the Gaussian process model provides a predictive distribution of computer model
 172 output at any untried value of θ given the existing output \mathbf{Y} (Sacks et al., 1989).
 173 We denote the resulting interpolation process by $\eta(\theta, \mathbf{Y})$ and call it an emula-
 174 tor. This emulator acts as an interpolator while at the same time providing a
 175 quantification of interpolation uncertainty.

176 Model Calibration Using Gaussian Random Field Model

177 Once an emulator $\eta(\theta, \mathbf{Y})$ is available, we model the observational data \mathbf{Z} ,

$$\mathbf{Z} = \eta(\mathbf{Y}, \theta) + \delta + \epsilon, \quad (1)$$

178 where $\epsilon \sim N(\mathbf{0}, \sigma^2 \mathbf{I})$ is independently and identically distributed observational
 179 error and δ is a data-model discrepancy term. δ is also modeled as a Gaussian
 180 process, thus $\delta \sim N(\mathbf{0}, \Sigma_d(\xi_d))$ with a spatial covariance matrix $\Sigma_d(\xi_d)$ between
 181 the locations $\mathbf{s}_1, \dots, \mathbf{s}_n$ and a vector of covariance parameters ξ_d . The details re-
 182 garding the specification of the covariance function are provided in Section 3.2.2.

183 This discrepancy term is crucial for parameter calibration (cf. Bayarri et al., 2007;
184 Bhat et al., 2010). Note that this problem is ill-posed without any prior informa-
185 tion for ξ_d , so an informative prior is necessary. Our inference for θ , ξ_d and σ^2 is
186 based on their resulting posterior distribution.

187 **2.2 Challenges with High-Dimensional Data**

188 High-dimensional datasets pose considerable computational challenges due to the
189 expensive likelihood function calculations that involve high-dimensional matrix
190 computations. This is an important issue because model output and observational
191 data in many fields, particularly climate science, tend to be high-dimensional. For
192 instance, in the calibration problem described in Section 4, the dimensionality
193 of the model output and the observational data is $n = 984$ in the 2-D case and
194 $n = 61,051$ in the 3-D case. The latter example involves prohibitive computations
195 with naïve implementations (discussed and explained below). For instance, with n -
196 dimensional climate model outputs at p different parameter settings, evaluation of
197 the likelihood function requires $\mathcal{O}(n^3 p^3)$ operations. Therefore numerical methods
198 such as Newton-Raphson or MCMC algorithms become infeasible. For the 3-D
199 case, this translates to 7.585×10^{13} flops of computations, which takes more than
200 3 hours for a high performance modern single-core processor.

201 **3 Model Calibration with High-Dimensional Spa-** 202 **tial Data**

203 We develop a dimension reduction approach based on spatial basis functions to in-
204 crease computational efficiency. Spatial basis functions can map high-dimensional
205 data into a low-dimensional space (Bayarri et al., 2007) and find a representation
206 of the probability model that results in a lower computational cost for likelihood
207 evaluations (Higdon et al., 2008; Bhat et al., 2012). Since there may be a trade-off
208 between parsimony and accurate inference, it is crucial to find a set of spatial ba-
209 sis functions that gives a computationally feasible likelihood formulation without
210 a considerable loss of information. Below, we review drawbacks to the current
211 approaches in the context of high-dimensional spatial data and propose a new
212 approach to overcome these limitations.

213 **3.1 Current Approaches**

214 A few different approaches to climate model calibration with multivariate com-
215 puter model outputs have been developed in recent years, including Bayarri et al.
216 (2007), Higdon et al. (2008), and Bhat et al. (2012). These approaches, however,
217 are not readily applicable to the 3D model output and observations we consider
218 here due to the following reasons. First, in spite of the gains in computational
219 efficiency likelihood evaluations remain computationally prohibitive. The compu-
220 tational cost of a single likelihood evaluation in the emulation step in Bhat et al.
221 (2012) scales as $\mathcal{O}(nJ^2)$ where J is the dimensionality of the basis matrix. In
222 Higdon et al. (2008), the computational cost scales with $\mathcal{O}(p^3 J_y^3)$ where J_y is the

223 number of principal components used to represent the data. For the 3D calibra-
224 tion problem we consider, n is 61,051, J is around 20,000 and J_y is around 20.
225 Second, the transformation based on the basis matrix may not be applicable to
226 two or three-dimensional spatial data. Using a wavelet transformation (Bayarri
227 et al., 2007) requires the same dyadic (a power of 2) number of data points for
228 each spatial dimension, and the data need to be on a regular grid without missing
229 values; irregular data and missing values are common in climate model calibration
230 problems. In addition, conducting Bayesian inference on the joint posterior dis-
231 tribution may pose difficulties, both computationally as well as in terms of prior
232 specification and identifiability issues. For example, Higdon et al. (2008) requires
233 estimating $4 \times J_y + 1$ parameters, which translates to an 81-dimensional distribution
234 for the 3-D case in Section 4.

235 **3.2 Reduced Dimensional Model Calibration**

236 Our method to overcome the aforementioned challenges relies on (i) represent-
237 ing the spatial field using principal components, and (ii) emulating each principal
238 component separately. Instead of using principal component basis to reduce the
239 complexity of matrix computation as in Higdon et al. (2008), we use it to map
240 the computer model outputs into a low-dimensional space and construct an em-
241 ulator in that space directly. Since the principal components are uncorrelated by
242 construction, we can build the emulator by constructing a 1-dimensional Gaus-
243 sian process for each principal component in parallel. Fitting Gaussian random
244 fields for each principal component requires estimation of only 5 parameters. The
245 likelihood evaluations involve covariance matrices of size $p \times p$. These features

246 allow us to construct the emulator in a computationally efficient and highly au-
 247 tomated manner. Moreover, since the principal component transformation can be
 248 applied to non-dyadic spatial data with irregular locations, it has a broader range
 249 of application than wavelet transformations. In the calibration step, we develop
 250 an approach to map the observational data into a low dimensional space.

251 3.2.1 Computer Model Emulation

252 The first step of this approach is to find the basis matrix for computer model
 253 output. We consider the computer model outputs as an n -dimensional dataset
 254 with p replications and find the principal component basis. Let \mathbf{M} denote the
 255 $p \times n$ matrix storing the computer model outputs $\mathbf{Y}_1, \dots, \mathbf{Y}_p$ such that

$$\mathbf{M} = \begin{pmatrix} \mathbf{Y}_1^T \\ \vdots \\ \mathbf{Y}_p^T \end{pmatrix}. \quad (2)$$

256 Following the standard process of finding principal components, we first preprocess
 257 the computer model outputs to make the column means of the matrix \mathbf{M} all
 258 0's. Applying singular value decomposition, we find the scaled eigenvectors $\mathbf{k}_1 =$
 259 $\sqrt{\lambda_1} \mathbf{e}_1, \dots, \mathbf{k}_p = \sqrt{\lambda_p} \mathbf{e}_p$ where $\lambda_1 > \lambda_2 > \dots > \lambda_p$ are the ordered eigenvalues
 260 and $\mathbf{e}_1, \dots, \mathbf{e}_p$ are the corresponding eigenvectors of the covariance matrix of \mathbf{M} ,
 261 where $J_y \ll p$ is the number of principal components that we decide to use in the
 262 emulator. One can choose the number of principal components by looking at the
 263 proportion of explained variation given by $\frac{\sum_{i=1}^{J_y} \lambda_i}{\sum_{i=1}^p \lambda_i}$. We define the basis matrix for
 264 computer model output by $\mathbf{K}_y = (\mathbf{k}_1, \dots, \mathbf{k}_{J_y})$.

For each parameter setting $\boldsymbol{\theta}_i$ ($i = 1, \dots, p$), the first J_y principal components $\mathbf{Y}_i^R = (Y_{i1}^R, \dots, Y_{iJ_y}^R)^T$ are computed by

$$\mathbf{Y}_i^R = (\mathbf{K}_y^T \mathbf{K}_y)^{-1} \mathbf{K}_y^T \mathbf{Y}_i.$$

265 Let $\mathbf{Y}^R = (\mathbf{Y}_1^R, \dots, \mathbf{Y}_p^R)^T$, hence each element of this matrix $\{\mathbf{Y}^R\}_{ij} = Y_{ij}^R$ is the
 266 j th principal component at the i th computer model parameter setting. Since the
 267 columns in \mathbf{K}_y are orthogonal, the principal components found here are uncorre-
 268 lated to each other and this leads us to a parallelized emulator construction that
 269 is similar to the wavelet transformation approach in Bayarri et al. (2007). For
 270 each j th principal component across the parameter settings (i.e. for each j th col-
 271 umn of \mathbf{Y}^R), we construct a Gaussian random field with the squared exponential
 272 covariance function such that

$$\text{Cov}(Y_{kj}^R, Y_{lj}^R) = \kappa_{y,j} \exp\left(-\sum_{i=1}^3 \frac{|\theta_{ik} - \theta_{il}|^2}{\phi_{y,ij}^2}\right) + \zeta_{y,j} 1(k=l) \quad (3)$$

273 with partial sill $\kappa_{y,j}$, nugget $\zeta_{y,j}$, and range parameters $\boldsymbol{\phi}_{y,j} = (\phi_{y,1j}, \phi_{y,2j}, \phi_{y,3j})^T$.
 274 Leave-10-percent-out cross-validation experiments with 50 different randomly gen-
 275 erated scenarios indicate that the squared exponential covariance shows a better
 276 fit than other alternatives such as exponential covariance.

We denote the collection of emulator parameters for each j th principal component by $\boldsymbol{\xi}_{y,j} = (\kappa_{y,j}, \zeta_{y,j}, \boldsymbol{\phi}_{y,j})^T$. One can construct the emulator by finding the MLE $\hat{\boldsymbol{\xi}}_{y,j}$ for each j separately. The emulator $\boldsymbol{\eta}(\boldsymbol{\theta}, \mathbf{Y}^R)$ is the collection of predictive processes of J_y principal components at $\boldsymbol{\theta}$ defined by the covariance function (3) and the MLEs $\hat{\boldsymbol{\xi}}_{y,1}, \dots, \hat{\boldsymbol{\xi}}_{y,J_y}$. Note that even though we constructed the em-

ulator in terms of the principal components, we can make a projection \mathbf{Y}^* in the original space at a new parameter setting $\boldsymbol{\theta}^*$ by computing

$$\mathbf{Y}^* = \mathbf{K}_y \boldsymbol{\eta}(\boldsymbol{\theta}^*, \mathbf{Y}^R).$$

277 To summarize, the emulation step uses the data $\mathbf{Y}_1^R, \dots, \mathbf{Y}_{J_y}^R$ of dimension p and
 278 compute MLEs $\hat{\boldsymbol{\xi}}_1, \dots, \hat{\boldsymbol{\xi}}_{J_y}$. Hence, the computational cost is reduced from $\mathcal{O}(n^3 p^3)$
 279 to $\mathcal{O}(J_y p^3)$ when compared to a naïve approach. The resulting fitted model is then
 280 used for the calibration step as described in the following section.

281 3.2.2 Computer Model Calibration

Using $\boldsymbol{\eta}(\boldsymbol{\theta}, \mathbf{Y}^R)$, the emulator for the principal components, we define the model for observational data by

$$\mathbf{Z} = \mathbf{K}_y \boldsymbol{\eta}(\boldsymbol{\theta}, \mathbf{Y}^R) + \mathbf{K}_d \boldsymbol{\nu} + \boldsymbol{\epsilon},$$

282 where $\mathbf{K}_d \boldsymbol{\nu}$ is a kernel convolution representation (Higdon, 1998) of the discrepancy
 283 $\boldsymbol{\delta}$. $\boldsymbol{\nu}$ is a vector of independent and identical Normal random variates at $J_d \ll n$
 284 locations, $\boldsymbol{\nu} \sim N(\mathbf{0}, \mathbf{I}_{J_d})$. $\mathbf{a}_1, \dots, \mathbf{a}_{J_d} \in \mathcal{S}$. We define the kernel basis by

$$(\mathbf{K}_d)_{ij} = \sqrt{\kappa_d} \exp \left(-\frac{g(s_{1i}, s_{2i}, a_{1j}, a_{2j})}{\phi_{d,1}} - \frac{|s_{3i} - a_{3j}|}{\phi_{d,2}} \right), \quad (4)$$

where s_{ki} and a_{kj} are the k th elements of \mathbf{s}_i and \mathbf{a}_j respectively. κ_d is the precision parameter determining the magnitude of discrepancy, and $\phi_{d,1}, \phi_{d,2} > 0$ are the range parameters specifying the bandwidth of kernels. The geodesic distance function measures the great circle distance between two points on the Earth's surface.

The function $g(s_{1i}, s_{2i}, a_{1j}, a_{2j})$ is given by

$$r \arccos(\sin(s_{2i}) \sin(a_{2j}) + \cos(\sin(s_{2i}) \cos(a_{2j}) \cos |s_{1i} - a_{1j}|),$$

285 where r is the radius of Earth (6378.388km). By following Higdon et al. (2008),
 286 the range parameters are pre-specified by scientific expert judgment; this reduces
 287 computations and identifiability issues. The kernel function in (4) yields a valid
 288 covariance under geodesic distance since it is strictly positive definite on a sphere
 289 (Gneiting, 2011). We assumed separability for distance along the surface and dis-
 290 tance along the depth. The resulting process is approximately twice differentiable
 291 (Zhu and Wu, 2010), which produces a reasonable model for discrepancy. Even
 292 though the discrepancy model implies an isotropic discrepancy process (Higdon,
 293 2002), the resulting process is flexible enough to capture the general trend in the
 294 discrepancy.

Instead of using the model (4) directly, we conduct calibration with reduced-
 dimensional data for computational efficiency. Let \mathbf{Z}^R be a reduced version of the
 original data such that

$$\mathbf{Z}^R = (\mathbf{K}^T \mathbf{K})^{-1} \mathbf{K}^T \mathbf{Z} = \begin{pmatrix} \boldsymbol{\eta}(\boldsymbol{\theta}, \mathbf{Y}^R) \\ \boldsymbol{\nu} \end{pmatrix} + (\mathbf{K}^T \mathbf{K})^{-1} \mathbf{K}^T \boldsymbol{\epsilon},$$

295 where $\mathbf{K} = (\mathbf{K}_y \ \mathbf{K}_d)$. The probability model of \mathbf{Z}^R is

$$\mathbf{Z}^R \sim N \left(\begin{pmatrix} \boldsymbol{\mu}_\eta \\ \mathbf{0} \end{pmatrix}, \begin{pmatrix} \Sigma_\eta & \mathbf{0} \\ \mathbf{0} & \kappa_d \mathbf{I}_{J_d} \end{pmatrix} + \sigma^2 (\mathbf{K}^T \mathbf{K})^{-1} \right), \quad (5)$$

296 where $\boldsymbol{\mu}_\eta$ and Σ_η are the mean and covariance given by the emulator $\boldsymbol{\eta}(\boldsymbol{\theta}, \mathbf{Y}^R)$.
 297 It is often helpful to apply singular value decomposition to \mathbf{K}_d and use the first
 298 $J_d^{PC} \ll J_d$ eigenvectors \mathbf{K}_d^{PC} in place of \mathbf{K}_d to find \mathbf{Z}^R . In addition to the obvious
 299 computational advantage, this often results in better inference since it corresponds
 300 to a regularized estimate given by ridge regression (see Hastie et al., 2009, pg. 66);
 301 this was corroborated by our extensive simulation studies.

302 Note that the term $\sigma^2(\mathbf{K}^T \mathbf{K})^{-1}$ in (5) automatically adjusts the contribution
 303 of each principal component to the calibration result. This can be illustrated by
 304 considering the model without the discrepancy, and the variance in the likelihood
 305 function is simply $\Sigma_\eta + \sigma^2(\mathbf{K}_y^T \mathbf{K}_y)^{-1}$. Since $(\mathbf{K}_y^T \mathbf{K}_y)^{-1}$ is a diagonal matrix and its
 306 i th diagonal element is the reciprocal of the i th eigenvalue, $(\mathbf{K}_y^T \mathbf{K}_y)^{-1}$ inflates the
 307 variance of principal components with small eigenvalues. Therefore, the principal
 308 components with smaller explained variance will have less effect on the calibration
 309 result.

310 We now briefly examine the covariance structure implied by our model. Using
 311 the leading J principal components, the covariance between computer model out-
 312 puts at two different spatial and parametric coordinates $(\mathbf{s}_1, \boldsymbol{\theta}_1)$ and $(\mathbf{s}_2, \boldsymbol{\theta}_2)$ can
 313 be written as

$$\begin{aligned} \text{Cov}(Y(\mathbf{s}_1, \boldsymbol{\theta}_1), Y(\mathbf{s}_2, \boldsymbol{\theta}_2)) &\approx \text{Cov}\left(\sum_{i=1}^J \lambda_i \mathbf{e}_i(\mathbf{s}_1) w_i(\boldsymbol{\theta}_1), \sum_{j=1}^J \mathbf{e}_j(\mathbf{s}_2) w_j(\boldsymbol{\theta}_2)\right) \\ &= \sum_{i=1}^J \sqrt{\lambda_i} \mathbf{e}_i(\mathbf{s}_1) \sqrt{\lambda_i} \mathbf{e}_i(\mathbf{s}_2) \text{Cov}(w_i(\boldsymbol{\theta}_1), w_i(\boldsymbol{\theta}_2)), \end{aligned}$$

where $\mathbf{e}_i(\cdot)$ is the i th eigenfunction satisfying

$$\int \text{Cov}(Y(\theta_1, \mathbf{s}_1), Y(\theta_2, \mathbf{s}_2)) \mathbf{e}_i(\mathbf{s}_2) d\mathbf{s}_1 = \lambda_i \mathbf{e}_i(\mathbf{s}_2) \text{Cov}(w_i(\boldsymbol{\theta}_1), w_i(\boldsymbol{\theta}_2)),$$

with the corresponding eigenvalue λ_i and the process of principal component $w_i(\cdot)$. The leading eigenfunctions give the best approximation among all possible orthogonal bases since it minimizes the total mean square error (Jordan, 1961). Since we can assume different covariance functions for each principal component process, our model can yield a non-separable space-parameter covariance function. In contrast, if we were to assume separability such that

$$\text{Cov}(Y(\boldsymbol{\theta}_1, \mathbf{s}_1), Y(\boldsymbol{\theta}_2, \mathbf{s}_2)) = C_s(\mathbf{s}_1, \mathbf{s}_2) C_\theta(\boldsymbol{\theta}_1, \boldsymbol{\theta}_2),$$

314 for some positive definite covariance functions C_s and C_θ , the covariance function
 315 for the i th principal component process becomes

$$\begin{aligned} \text{Cov}(w_i(\boldsymbol{\theta}_1), w_i(\boldsymbol{\theta}_2)) &= \text{Cov}\left(\int Y(\boldsymbol{\theta}_1, \mathbf{s}_1) \mathbf{e}_i(\mathbf{s}_1) d\mathbf{s}_1, \int Y(\boldsymbol{\theta}_2, \mathbf{s}_2) \mathbf{e}_i(\mathbf{s}_2) d\mathbf{s}_2\right) \\ &= \int \mathbf{e}_i(\mathbf{s}_1) \left(\int \text{Cov}(Y(\boldsymbol{\theta}_1, \mathbf{s}_1), Y(\boldsymbol{\theta}_2, \mathbf{s}_2)) \mathbf{e}_i(\mathbf{s}_2) d\mathbf{s}_2 \right) d\mathbf{s}_1 \\ &= C_\theta(\boldsymbol{\theta}_1, \boldsymbol{\theta}_2) \int \mathbf{e}_i(\mathbf{s}_1) \int \text{Cov}(\mathbf{s}_1, \mathbf{s}_2) \mathbf{e}_i(\mathbf{s}_2) d\mathbf{s}_2 d\mathbf{s}_1 \\ &= C_\theta(\boldsymbol{\theta}_1, \boldsymbol{\theta}_2) \lambda_i. \end{aligned}$$

316 The separability assumption therefore results in a restrictive covariance structure
 317 such that the correlation function for all principal component processes are the
 318 same. Hence even though our reduced dimensional approach utilizes a covariance
 319 that is easy to specify, it provides a richer class of covariance functions than a sepa-

320 rable covariance structure. Our cross-validation studies show that our assumption
 321 is adequate for emulating the computer model.

322 Priors

323 We estimate the joint density of $\boldsymbol{\theta}$, κ_d , and σ^2 using the Metropolis-Hastings al-
 324 gorithm. Following Bayarri et al. (2007), we allow for additional flexibility by
 325 estimating the partial sill parameters $\kappa_{y,1}, \dots, \kappa_{y,J_y}$ for the emulator. Prior spec-
 326 ification for the parameters in the observational model is straightforward. The
 327 discrepancy variance κ_d and the observational error variance σ^2 receive inverse-
 328 gamma priors with small shape parameter values. The prior for each parameter
 329 being calibrated is a uniform distribution over a broad range or determined by sci-
 330 entific knowledge. In order to stabilize the inference, we put an informative prior
 331 to encourage $\kappa_{y,1}, \dots, \kappa_{y,J_y}$ to vary around their estimated values in the emulation
 332 stage.

333 Computing

334 The computational costs may be summarized as follows:

- 335 1. Find the basis matrix $\mathbf{K}_y = (\sqrt{\lambda_1}\mathbf{e}_1, \dots, \sqrt{\lambda_{J_y}}\mathbf{e}_{J_y})$ by computing the singu-
 336 lar value decomposition of \mathbf{M} in (2). This computation is of order $\mathcal{O}(n^3)$,
 337 but it needs to be done only once.
- 338 2. Compute \mathbf{Y}_R where its i th row is the transpose of $(\mathbf{K}_y^T \mathbf{K}_y)^{-1} \mathbf{K}_y^T \mathbf{Y}_i$.
- 339 3. Construct a Gaussian random field for each column of \mathbf{Y}_R by finding the
 340 MLE $\hat{\boldsymbol{\xi}}_{y,i}$ for each $i = 1, \dots, J_y$. The computational cost is of order $\mathcal{O}(p^3)$
 341 for each likelihood evaluation.

- 342 4. Compute $\mathbf{Z}_R = (\mathbf{K}^T \mathbf{K})^{-1} \mathbf{K}^T \mathbf{Z}$. The computational complexity of this step
343 is $\mathcal{O}((J_y + J_d)^3)$.
- 344 5. Using Metropolis-Hastings, draw an MCMC sample of $\boldsymbol{\theta}$, σ^2 , κ_d and $\kappa_{y,1}, \dots, \kappa_{y,J_y}$
345 from the joint posterior distribution based on the model in (5). The compu-
346 tational cost for each likelihood evaluation is of order $\mathcal{O}((J_y + J_d)^3)$.
- 347 The overall cost of our implementation is $\mathcal{O}(pJ_y^3)$ for the emulation step and
348 $\mathcal{O}((J_y + J_d)^3)$ for the calibration step.

349 4 Implementation Details

350 Our goal is to build an emulator based on spatial output from UVic ESCM and to
351 calibrate vertical ocean diffusivity (K_{bg}) using ocean potential temperature data.
352 The UVic ESCM runs are 3-dimensional patterns of the mean ocean potential
353 temperature over 1955–2006 at $p = 250$ parameter settings. The parameters con-
354 trolling model outputs are vertical ocean diffusivity (K_{bg}), anthropogenic aerosol
355 scaling factor (A_{scl}), and climate sensitivity (C_s). Note that we converted long-
356 wave radiation feedback factor, which is one of the original input parameters for
357 UVic, into C_s using a simple spline fit. We refer to Srivier et al. for the design
358 points and more details of this ensemble runs.

359 To avoid the problem related to model artifacts and sparse sampling, we ex-
360 cluded data beyond 60°N and 80°S and 3000m in depth (Key et al., 2004; Schmit-
361 tner et al., 2009; Bhat et al., 2012). UVic ESCM outputs are on a 77 (latitude) ×
362 100 (longitude) × 13 (depth) grid, but the number of locations that have non-
363 missing observations is 65,595. The missing values occur because there is no ocean

364 at the locations in the UVic ESCM representation.

365 The observational data is on a 180 (latitude) \times 360 (longitude) \times 33 (depth)
366 grid, and we remap this observed data into the Uvic model grid using a linear in-
367 terpolation. This results in a relatively small reduction of data points to 61,051 data
368 points. The model output locations considered in our modeling are also adjusted
369 accordingly. We convert the observed in-situ temperature field into potential tem-
370 perature field in order to (i) have the same measurement unit with UVic ESCM
371 output and (ii) adjust the effect of pressure on ocean temperature. We obtain
372 potential temperature from the in-situ temperature (Locarnini et al., 2010) and
373 salinity fields (Antonov et al., 2010) using UNESCO equation of state (UNESCO,
374 1981) following Bryden (1973) and Fofonoff (1977). During the conversion proce-
375 dure, we assume a simplified ocean pressure field varying as a function of latitude
376 and depth (Lovett, 1978). We apply our method to data at three different aggre-
377 gation levels. In the 1-D case, we compute the vertical means at $n = 13$ different
378 depth points (Goes et al., 2010). In the 2-D case, the longitudinal means are
379 computed at $n = 984$ latitude and depth points (Bhat et al., 2012). We use the
380 original pattern without any aggregation in the 3-D case ($n = 61,051$). The num-
381 ber of principal components is determined to have more than 90% of the explained
382 variation. The number of components is 5 for the 1-D, 10 for the 2-D, and 20 for
383 the 3-D case. We also tried to use 10 principal components for the 1-D, 20 for
384 the 2-D, and 30 for the 3-D case to have more than 95% explained variation, but
385 could not find any improvement in the calibration result.

386 We use all 250 design points in the parameter space to build the emulator.
387 We fix C_s and A_{scl} at the default values of the UVic ESCM in the calibration
388 stage and made an inference only for K_{bg} . The default values are 1 for A_{scl} and

389 3.81879 for C_s . One may choose to integrate out these two parameters, but since
 390 the ocean temperature field lacks strong information about A_{scl} and C_s , their es-
 391 timated posterior densities are overly dispersed. This introduces unnecessary bias
 392 in the estimate of K_{bg} due to the highly non-linear relationship between climate
 393 parameters (Olson et al., 2012), thus we decided not to integrate out those two
 394 parameters.

395 By following Bhat et al. (2012), we assume a flat prior with a broad range for
 396 K_{bg} , from 0.05 to 0.55. The variance for the observational error (σ^2) and the model
 397 discrepancy (κ_d) receive inverse-Gamma priors, and we denote them by $\text{IG}(a_\nu, b_\nu)$
 398 and $\text{IG}(a_z, b_z)$. We set the shape parameters for them by $a_\nu = 2$ and $a_z = 2$. To
 399 check the sensitivity of our approach to prior specifications, we tried four different
 400 combinations, (2, 2), (2, 100), (100, 2), and (100, 100) for b_ν and b_s . The emulator
 401 variances $\kappa_{y,1}, \dots, \kappa_{y,J_y}$ also receive inverse-Gamma priors with a shape parameter
 402 of 5. The scale parameters are determined to have modes at their estimated values
 403 in the emulation stage. Because of parameter identifiability problems which in turn
 404 affected computation, we fixed the range parameter for depth at 3000m and for
 405 surface as 2500km. We found that a wide range of the different settings for these
 406 parameters gave the same inference result for K_{bg} and hence our particular choices
 407 did not affect the results. The number of knot locations for the discrepancy kernel
 408 is 800 in the 3D case, 80 in the 2D case, and 13 in the 1D case. The number of
 409 principal components used for the discrepancy is 200 in the 3D case, 20 in the 2D
 410 case, and 5 in the 1D case. The number of principal components was determined
 411 using standard practice – by ensuring that at least 95% of the variability in the
 412 data was explained in each case. In order to check the robustness of our results, we
 413 tried different numbers of principal components. For example, when we increased

414 the number of principal components to 300 in the 3D case, 30 in the 2D case and
415 8 in the 1D case we found that we obtained virtually identical calibration results.

416 **5 Results**

417 **5.1 Computational Benefit**

418 The biggest challenge in the considered analysis is the computational cost of eval-
419 uating the likelihood function in the 3-D case, which requires dealing with 61,051-
420 dimensional spatial datasets. To our knowledge, current approaches cannot ad-
421 dress this problem with reasonable computational effort (discussed below). The
422 required number of principal components is about 20 for the 3-D case for reason-
423 able accuracy and this means we still need to invert a $5,000 \times 5,000$ covariance
424 matrix for the likelihood evaluation in the emulation stage for the method due
425 to Higdon et al. (2008). Moreover, the number of parameters to be estimated is
426 81, and this requires updating more than ten parameter blocks for each iteration
427 of MCMC to obtain a reasonably well-mixed chain. The method of Bhat et al.
428 (2012) requires multiplication of a $J \times 61,501$ matrix into another $61,501 \times J$ ma-
429 trix in the likelihood evaluation with certain number of knots J , and this makes
430 the likelihood evaluation computationally prohibitive.

431 The computational time in emulation stage for the 1-dimensional, 2-dimensional
432 and 3-dimensional cases for different methods are illustrated in Figure 1. The com-
433 puting time shown in the figure is for a system with Intel Xeon E5450 Quad-Core
434 3.0 GHz and based on the computational complexity for matrix operations in-
435 volved in each method. We assume that each method has been implemented using

436 Markov chain Monte Carlo maximum likelihood estimation with 25,000 iterations.
437 In order to consider the dimensionality of parameter space in our comparison, we
438 assume that five parameters are updated as a block in each MCMC run. Our
439 method can deal with the 3-D case with a reasonable computational cost. We
440 note that while we did not include this in our comparisons, parallel computing
441 may further speed up computations for our approach. Since there are 81 param-
442 eters in the approach due to Higdon et al. (2008), the method requires updating
443 17 parameter blocks for each MCMC iteration in the 3D case.

444 **5.2 The Effect of Data Aggregation on Climate Model Cal-** 445 **ibration**

446 In order to study the effect of data aggregation on climate model calibration,
447 we conducted a study with pseudo-observational data. The simulated data are
448 generated as follows:

- 449 1. Choose the 3-D pattern of UVic ESCM output with $K_{bg} = 0.2$, $A_{scl} = 1.5$,
450 and $C_s = 3.975975$ as the synthetic truth.
- 451 2. Compute three different 3-D patterns of residuals between the observational
452 data and the UVic model outputs with $K_{bg} = 0.1$, $K_{bg} = 0.2$, and $K_{bg} = 0.3$.
453 The values for A_{scl} and C_s are the same as in Step 1. Average them over
454 each location to compute a pseudo-residual. This is a more realistic and
455 challenging residual than one obtained by simulation from a simple error
456 model, for example a realization from a Gaussian process model. For brevity,
457 we describe here just this most challenging case; our methods worked even

458 better in terms of posterior variance when error processes were assumed to
459 be simpler.

460 3. Superimpose the pseudo residual on the synthetic truth to construct pseudo
461 observational data in 3-D.

462 4. Aggregate the 3-D pseudo observational data into 2-D and 1-D by integrating
463 the ocean temperature with respect to water volume.

464 The calibration results based on this simulated example is shown in Figure 2. The
465 sensitivity test indicates that the posterior distribution of K_{bg} in the 1-D and the
466 2-D cases rely on the specification of priors. This deep uncertainty is drastically
467 reduced when the full data set (3-D) is used. A comparison result based on the real
468 data from Ocean Atlas 2009 is shown in Figure 3. As in the simulated example, the
469 calibration results based on the 3-D data are more robust to the prior specification.

470 Using the full pattern of the 3-D data has important benefits as it drastically
471 reduces the deep uncertainty due to different prior specifications. We hypothesize
472 that this is because the full non-aggregated spatial patterns contain more infor-
473 mation about both the observational error and the discrepancy. In order to reflect
474 the uncertainty due to prior choice to our density estimate for K_{bg} , we show in
475 Figure 4 the posterior distributions when the prior is assumed to be with equal
476 probability any one of the 4 priors considered, along with the resulting AMOC
477 projections. We define AMOC projection as the annual maximum value of the
478 meridional overturning streamfunction in the Atlantic between 0° and 70°N . The
479 corresponding projections for AMOC change between 1970 to 1999 mean and 2070
480 to 2099 mean indicate that the unaggregated pattern gives a much narrower 95%
481 predictive interval than the aggregated ones. Therefore, data aggregation increases

482 the deep uncertainty surrounding AMOC projection, and using unaggregated data
483 reduces uncertainty regarding the future behavior of the AMOC.

484 **6 Discussion**

485 **6.1 Summary**

486 We propose a computer model calibration approach that is computationally effi-
487 cient even when dealing with high-dimensional data. By exploiting the orthog-
488 onality of a principal components decomposition of the data, this method can
489 keep the computational cost affordable for high-dimensional data with more than
490 60,000 spatial locations and 250 parameter settings. We apply this method to
491 the problem of calibrating a climate model parameter in an Earth System Model
492 of Intermediate complexity based on observations of the potential temperature.
493 The calibration results show that using 3-D data reduces the uncertainty about
494 K_{bg} and is more robust to various prior specifications than calibration based on
495 2-D or 1-D aggregated versions of the data. The results suggest that using unag-
496 gregated data is valuable for reducing deep uncertainty associated with different
497 priors. Our simulated examples show that our approach can handle complicated
498 model-observation discrepancies. The method can be easily extended to allow for
499 calibration with multiple tracers – we can simply consider the variance-covariance
500 matrix for all tracers and use its principal components to build an emulator.

501 6.2 Caveats

502 A general issue with principal components is also worth considering in this con-
503 text: the principal components for the computer model outputs are selected based
504 on explained variation, and thus there is no guarantee that these leading principal
505 components carry the most important information about the climate parameters.
506 However, our extensive study of the effect of changing the number of principal
507 components suggests that this is not problematic in our context. Our results are
508 consistent with the recent theoretical results in Artemiou and Li (2009) that sug-
509 gest that there is a low probability that other (non-leading) principal components
510 will have a strong correlation with the climate parameters. We hypothesize that
511 our principal components based approach does not lose valuable information about
512 the climate parameters. In the discrepancy model, one important simplifying as-
513 sumption is the separability between surface and depth effects. Our simulated
514 example shows that the separability assumption provides a good approximation
515 to the realistic discrepancy process. Non-separable covariance function that com-
516 bines geodesic distance and Euclidean distance remains as an avenue of ongoing
517 and alive research and subject of future work. Furthermore, our study of calibra-
518 tion with simulated examples shows that even though the number of K_{bg} settings at
519 which the model is run is relatively sparse, there is enough information to reliably
520 calibrate K_{bg} based on our emulator.

521 Our study is also subject to usual caveats with respect to scientific conclu-
522 sions. First, we ignore the interpolation uncertainty when we compute the density
523 of AMOC projection based on the density of K_{bg} . Second, the result is based on
524 a single data set, and thus we cannot fully evaluate the effect of structural uncer-

525 tainty due to the model-observation discrepancy and unresolved natural variability
526 cannot be accounted for; this variability could impact conclusions as well (Olson
527 et al.). These caveats, of course, apply to almost all existing approaches to climate
528 model calibration and projection.

529 **Acknowledgments**

530 This work was supported by NSF through the Network for Sustainable Climate
531 Risk Management (SCRiM) under NSF cooperative agreement GEO-1240507.

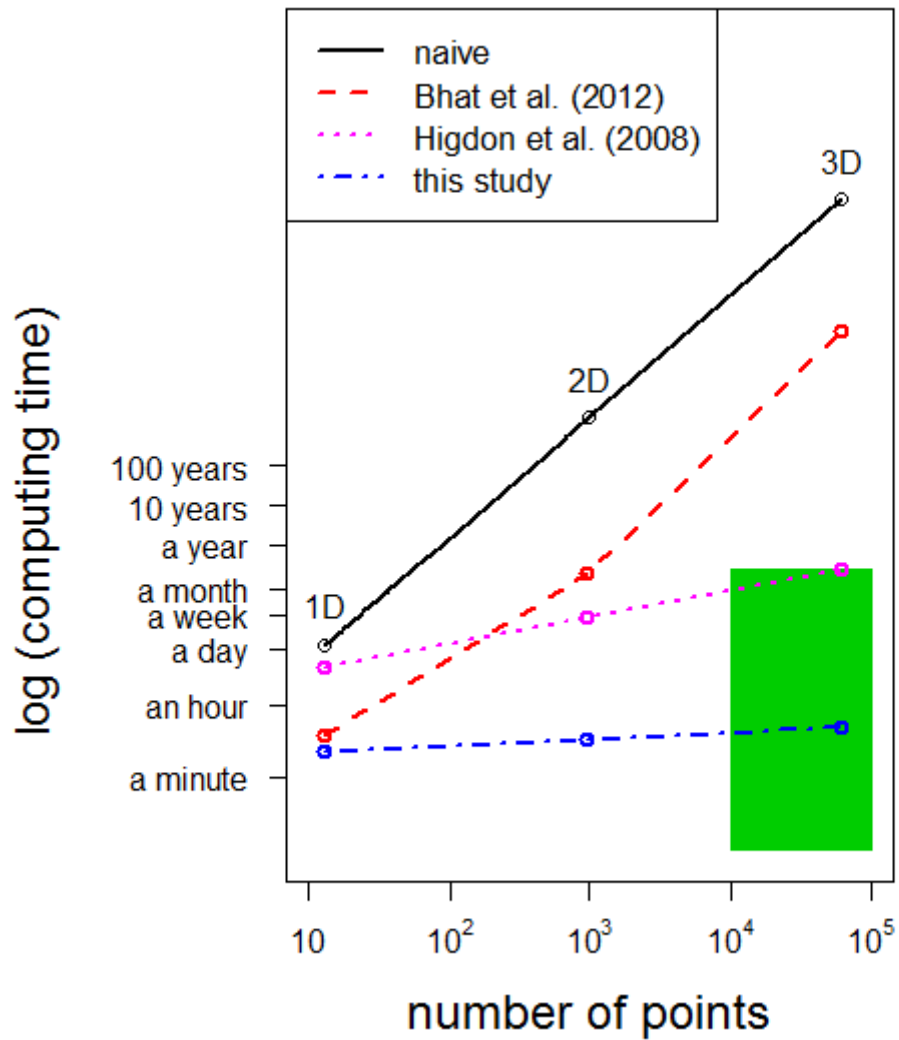


Figure 1: Comparison of computational costs for the emulation step between the current approaches and the new approach. The green box near the bottom right corner shows computing times that are practical, ranging from one second to three months.

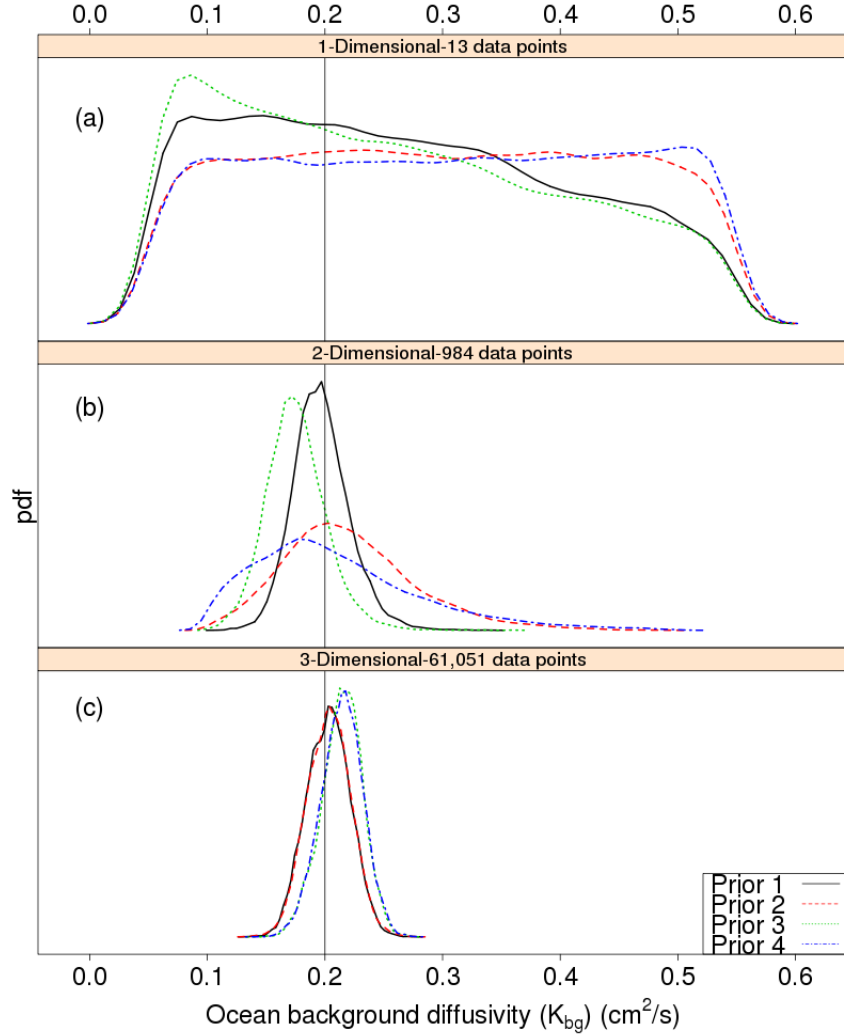


Figure 2: Prior sensitivity test in the simulated example. Calibration of K_{bg} value based on (a) 1-D depth profile (upper panel), (b) 2-D latitude-depth pattern (middle panel) (c) 3-D non-aggregated data (lower panel). Each line represents posterior density from four different priors: $(b_v = 2, b_z = 2)$ (Prior 1, solid line), $(b_v = 2, b_z = 100)$ (Prior 2, dashed line), $(b_v = 100, b_z = 2)$ (Prior 3, dotted line), and $(b_v = 100, b_z = 100)$ (Prior 4, dot-dashed line). The solid vertical line represents the true value of K_{bg} in the synthetic truth.

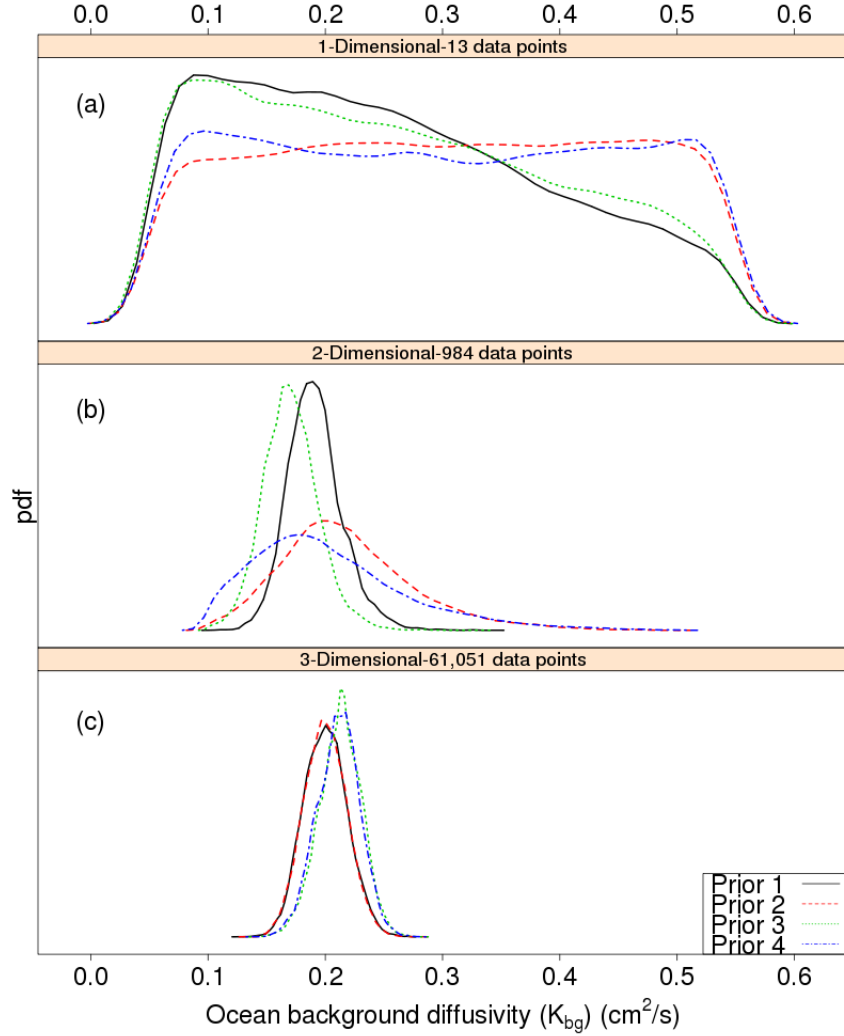


Figure 3: Prior sensitivity test using observational data from the World Ocean Atlas 2009. Calibration results based on (a) 1-D depth profile (upper panel), (b) 2-D latitude-depth pattern (middle panel) (c) 3-D non-aggregated data (lower panel). Each line represents posterior density from four different priors: ($b_v = 2, b_z = 2$) (Prior 1, solid line), ($b_v = 2, b_z = 100$) (Prior 2, dashed line), ($b_v = 100, b_z = 2$) (Prior 3, dotted line), and ($b_v = 100, b_z = 100$) (Prior 4, dot-dashed line).

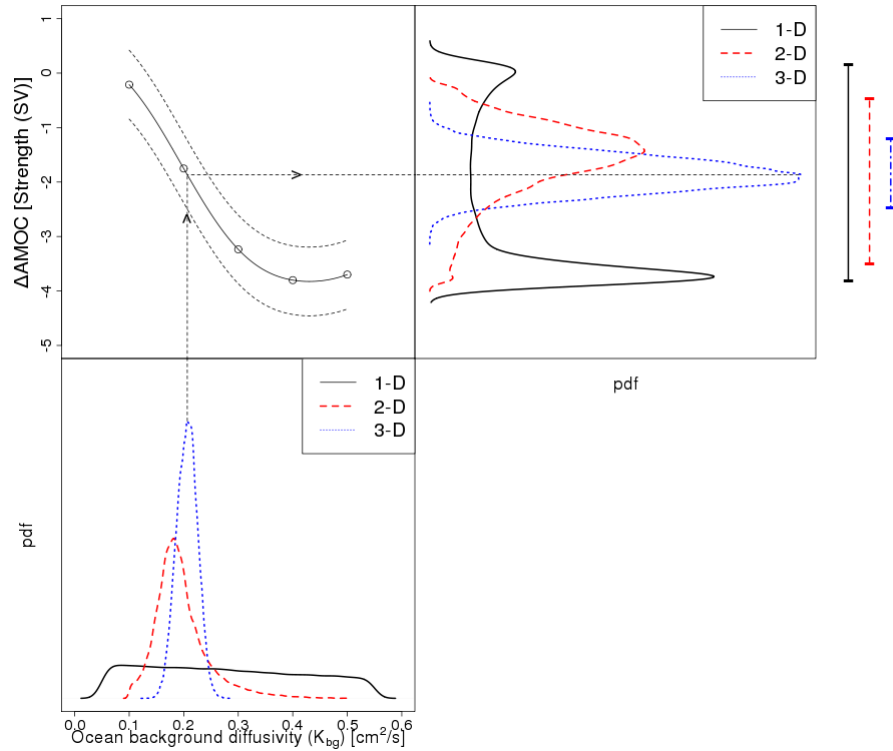


Figure 4: Combined posterior densities of K_{bg} from different prior specifications (lower left), the relationship between K_{bg} and projected AMOC change of the 2070 - 2099 mean from the 1970 - 1999 mean (upper left), and the resulting AMOC change projections (upper right) using 1-D (solid line), 2-D (dashed line) and 3-D (dotted line) data with their 95% credible intervals (bars at the right)

532 **References**

- 533 R. Alley, T. Berntsen, N. L. Bindoff, Z. Chen, A. Chidthaisong, P. Friedlingstein,
534 J. Gregory, G. Hegerl, M. Heimann, B. Hewitson, F. Joos, J. Jouzel, V. Kattsov,
535 U. Lohmann, M. Manning, T. Matsuno, M. Molina, N. Nicholls, J. Over-
536 peck, D. Qin, G. Raga, V. Ramaswamy, J. Ren, M. Rusticucci, S. Solomon,
537 R. Somerville, T.F Stocker, P. Stott, P. Whetton, R.A. Wood, and D. Wratt.
538 *Climate Change 2007: The Physical Science Basis: Summary for Policymak-*
539 *ers: Contribution of Working Group I to the Fourth Assessment Report of the*
540 *Intergovernmental Panel on Climate Change*, 2007. IPCC.
- 541 J.I. Antonov, D. Seidov, T.P. Boyer, R.A. Locarnini, A.V. Mishonov, H.E. Garcia,
542 O.K. Baranova, M.M. Zweng, and D.R. Johnson. *World Ocean Atlas 2009,*
543 *Volume 2: Salinity*, S. Levitus, Ed., NOAA Atlas NESDIS 69, US Government
544 Printing Office, Washington, DC. page 184, 2010.
- 545 A. Artemiou and B. Li. On principal components and regression: A statistical
546 explanation of a natural phenomenon. *Statistica Sinica*, 19(4):1557–1565, 2009.
- 547 M.J. Bayarri, J.O. Berger, J. Cafeo, G. Garcia-Donato, F. Liu, J. Palomo, R.J.
548 Parthasarathy, R. Paulo, J. Sacks, and D. Walsh. Computer model validation
549 with functional output. *The Annals of Statistics*, 35(5):1874–1906, 2007.
- 550 K.S. Bhat, M. Haran, and M. Goes. Computer model calibration with multivari-
551 ate spatial output: A case study. *Frontiers of Statistical Decision Making and*
552 *Bayesian Analysis*, pages 168–184, 2010.
- 553 K.S. Bhat, M. Haran, R. Olson, and K. Keller. Inferring likelihoods and climate

- 554 system characteristics from climate models and multiple tracers. *Environmetrics*,
555 23(4):345–362, 2012.
- 556 F. Bryan. Parameter sensitivity of primitive equation ocean general circulation
557 models. *Journal of Physical Oceanography*, 17(7):970–985, 1987.
- 558 H. L. Bryden. New polynomials for thermal expansion, adiabatic temperature gra-
559 dient and potential temperature of sea water. *Deep Sea Research and Oceanog-
560 graphic Abstracts*, 20(4):401–408, 1973.
- 561 N. Cressie. Models for spatial processes. *Statistical Methods for Physical Science*,
562 28(C):93–124, 1994.
- 563 D. Drignei, C.E. Forest, and D. Nychka. Parameter estimation for computationally
564 intensive nonlinear regression with an application to climate modeling. *The
565 Annals of Applied Statistics*, 2(4):1217–1230, 2008.
- 566 N.P. Fofonoff. Computation of potential temperature of seawater for an arbitrary
567 reference pressure. *Deep Sea Research*, 24(5):489–491, 1977.
- 568 C.E. Forest, P.H. Stone, and A.P. Sokolov. Constraining climate model parameters
569 from observed 20th century changes. *Tellus A*, 60(5):911–920, 2008.
- 570 A. Gnanadesikan. A simple predictive model for the structure of the oceanic
571 pycnocline. *Science*, 283(5410):2077–2079, 1999.
- 572 T. Gneiting. Strictly and non-strictly positive definite functions on spheres. *arXiv
573 preprint arXiv:1111.7077*, 2011.

- 574 M. Goes, N.M. Urban, R. Tonkonojenkov, M. Haran, A. Schmittner, and K. Keller.
575 What is the skill of ocean tracers in reducing uncertainties about ocean diapyc-
576 nal mixing and projections of the Atlantic Meridional Overturning Circulation?
577 *Journal of Geophysical Research: Oceans*, 115(C12006), 2010.
- 578 T. Hastie, R. Tibshirani, and J. Friedman. *The elements of statistical learning:
579 data mining, inference, and prediction*. Springer, 2009.
- 580 D. Higdon. A process-convolution approach to modelling temperatures in the
581 North Atlantic Ocean. *Environmental and Ecological Statistics*, 5(2):173–190,
582 1998.
- 583 D. Higdon. Space and space-time modeling using process convolutions. *Quantita-
584 tive methods for current environmental issues*, 2002.
- 585 D. Higdon, J. Gattiker, B. Williams, and M. Rightley. Computer model calibration
586 using high-dimensional output. *Journal of the American Statistical Association*,
587 103(482):570–583, 2008.
- 588 K.L. Jordan. Discrete representations of random signals. *technical report*, 1961.
589 Massachusetts Institute of Technology Technical Report 378.
- 590 Klaus Keller, Matt Hall, Seung-Rae Kim, David F Bradford, and M Oppenheimer.
591 Avoiding dangerous anthropogenic interference with the climate system. *Cli-
592 matic Change*, 73(3):227–238, 2005.
- 593 Klaus Keller, Curtis Deutsch, Matthew G Hall, and David F Bradford. Early
594 detection of changes in the north atlantic meridional overturning circulation:

- 595 implications for the design of ocean observation systems. *Journal of Climate*,
596 20(2):145–157, 2007.
- 597 M.C. Kennedy and A. O’Hagan. Bayesian calibration of computer models. *Journal*
598 *of the Royal Statistical Society. Series B (Statistical Methodology)*, 63(3):425–
599 464, 2001.
- 600 R.M. Key, A. Kozyr, CL Sabine, K. Lee, R. Wanninkhof, JL Bullister, RA Feely,
601 FJ Millero, C. Mordy, and T.H. Peng. A global ocean carbon climatology:
602 Results from Global Data Analysis Project (GLODAP). *Global Biogeochemical*
603 *Cycles*, 18(GB4031), 2004.
- 604 F. Liu, MJ Bayarri, and JO Berger. Modularization in bayesian analysis, with
605 emphasis on analysis of computer models. *Bayesian Analysis*, 4(1):119–150,
606 2009.
- 607 RA Locarnini, AV Mishonov, JI Antonov, TP Boyer, HE Garcia, OK Baranova,
608 MM Zweng, and DR Johnson. *World Ocean Atlas 2009, Volume 1: Tempera-*
609 *ture*, S. Levitus, Ed., NOAA Atlas NESDIS 68, US Government Printing Office,
610 Washington, DC. page 184, 2010.
- 611 J. R. Lovett. Merged seawater sound-speed equations. *The Journal of the Acous-*
612 *tical Society of America*, 63:1713–1718, 1978.
- 613 R. Olson, R. Sriver, M. Haran, W. Chang, N.M. Urban, and K. Keller. What is the
614 effect of unresolved internal climate variability on climate sensitivity estimates?
615 *Journal of Geophysical Research: Atmospheres*. under revision.
- 616 R. Olson, R. Sriver, M. Goes, N.M. Urban, H.D. Matthews, M. Haran, and

- 617 K. Keller. A climate sensitivity estimate using Bayesian fusion of instrumen-
618 tal observations and an Earth System model. *Journal of Geophysical Research:*
619 *Atmospheres*, 117(D04103), 2012.
- 620 J. Rougier. Comment on article by Sanso et al. *Bayesian Analysis*, 3(1):45–56,
621 2008.
- 622 J. Sacks, W.J. Welch, T.J. Mitchell, and H.P. Wynn. Design and analysis of
623 computer experiments. *Statistical Science*, 4(4):409–423, 1989.
- 624 B. Sanso and C.E. Forest. Uncertainty quantification: Statistical calibration of
625 climate system properties. *Applied Statistics*, 58(4):485–03, 2009.
- 626 A. Schmittner, N.M. Urban, K. Keller, and D. Matthews. Using tracer observations
627 to reduce the uncertainty of ocean diapycnal mixing and climate–carbon cycle
628 projections. *Global Biogeochemical Cycles*, 23(4), 2009.
- 629 L. Sriver, M. Nathan, R. , we, and K. Keller. Toward a physically plausible upper
630 bound of sea-level rise projections. *Climate Change*, 115(3–4):893–902.
- 631 UNESCO. Tenth report of the joint panel on oceanographic tables and standards.
632 *Technical report*, 1981. UNESCO Technical Reports on Marine Science 36.
- 633 A.J. Weaver, M. Eby, E.C. Wiebe, C.M. Bitz, P.B. Duffy, T.L. Ewen, A.F. Fan-
634 ning, M.M. Holland, A. MacFadyen, and H.D. Matthews. The UVic Earth Sys-
635 tem Climate Model: Model description, climatology, and applications to past,
636 present and future climates. *Atmosphere-Ocean*, 39(4):361–428, 2001.
- 637 C. Wunsch and R. Ferrari. Vertical mixing, energy, and the general circulation of
638 the oceans. *Annual Review of Fluid Mechanics*, 36:281–314, 2004.

639 Z. Zhu and Y. Wu. Estimation and prediction of a class of convolution-based
640 spatial nonstationary models for large spatial data. *Journal of Computational*
641 *and Graphical Statistics*, 19(1):74–95, 2010.